Simultaneous Determination of the Spin Polarizations of Noble-Gas and Alkali-Metal Atoms Based on the Dynamics of the Spin Ensembles

Kai Wei,[1,2,*] Tian Zhao,[1,2] Xiujie Fang,[1,2] Hairong Li,[1,2] Yueyang Zhai●,[1,2] Bangcheng Han,[1,2] and Wei Quan[3,4,5,†]

[1] *School of Instrumentation and Optoelectronic Engineering, Beihang University, Beijing 100191, China*
[2] *Quantum Sensing Center, Zhejiang Laboratory, Hangzhou 310000, China*
[3] *Beijing Advanced Innovation Center for Big Data-Based Precision Medicine, Beihang University, Beijing 100191, China*
[4] *Research Institute of Frontier Science, Beihang University, Beijing 100191, China*
[5] *Beijing Academy of Quantum Information Sciences, Beijing, 100193, China*

We demonstrate a method for simultaneously measuring the spin polarizations of noble-gas and alkali-metal atoms. Under a low magnetic field, the polarized alkali-metal and noble-gas spin ensembles exhibit novel dynamics in the self-compensation and resonance regimes, which can be used to measure the polarizations. We perform this method on a K-Rb-^{21}Ne comagnetometer with various operation temperatures and pump-light intensities. The polarization of alkali-metal electrons from 0.245 to 0.964 and the polarization of noble-gas nuclear spins from 0.01 to 0.065 are measured with relative uncertainties less than 12.4%. The measured polarizations are consistent with the theoretical model and are also verified by the traditional polarization-measurement method.

I. INTRODUCTION

Hyperpolarized noble gases through spin-exchange optical pumping have been used in a variety of scientific and medical applications, including tests of fundamental symmetries [1,2], searches for exotic spin-dependent interactions [3,4], magnetic resonance imaging [5,6], neutron polarizers and analyzers [7], and inertial navigation [8,9]. In some of these applications, magnetic field noise is the dominant noise and is suppressed by the self-compensation operation [2,4,8], the suppressing ability of which is determined by the noble-gas and alkali-metal polarizations [8,10]. Thus, it is important to measure the polarizations to optimize the suppressing ability. Additionally, in order to study the polarization limits and efficiencies of noble-gas and alkali-metal atoms in hybrid optical pumping, it is necessary to measure the polarizations [11,12].

The conventional methods to measure the polarization of noble-gas nuclear spins are nuclear-magnetic-resonance (NMR) detection [13,14] and the electron-paramagnetic-resonance (EPR) frequency-shift method [15,16]. In the NMR detection method, the NMR signal induced by the tipping of the noble-gas spins is detected by the pickup coils to obtain the polarization, which requires additional tipping rf coils and accurately calibrated pickup coils. As

for the EPR frequency-shift method, to measure the shift in the EPR frequency of alkali-metal atoms upon the reversal of the noble-gas spins, a double-feedback scheme locking the magnetic holding field to the resonance of the alkali-metal atoms and the technique of adiabatic fast passage are required. To measure the polarization of alkali-metal electrons, the conventional method using rf spectroscopy on the Faraday rotation [16–18] is applied, which requires a strong rf field to sweep through the Zeeman resonances of alkali-metal atoms. Another method based on the fitting of the transient buildup and decay of polarization is also used [19,20]; however, the accuracy is affected by the distortion of the transient signal and the change in the slowing-down factor during the buildup-and-decay process. Furthermore, a method based on the frequency shift of the noble-gas nuclear-spin precession (FSNP) due to the flipping of the alkali-metal spins is used [21] but this causes the depolarization of noble-gas nuclear spins.

Here, we demonstrate a method for measuring the spin polarizations of noble-gas and alkali-metal atoms based on the dynamics of the spin ensembles. Utilizing the novel dynamics of the spin-polarized alkali-metal and noble-gas ensembles under a low magnetic field, this method can be used to simultaneously measure the polarizations, simplifying the previous separated measurement procedure. This method operates under low-magnetic-field conditions, requiring no complex magnetic field coil or feedback loop; hence, this simplified configuration

---

*weikai@buaa.edu.cn
†quanwei@buaa.edu.cn

044027-1

is suitable for miniaturized devices. In addition, this method causes no depolarization of the noble-gas or alkali-metal spins and can be used in real-time polarization measurement.

II. THEORY

In the alkali-metal noble-gas comagnetometer, the alkali-metal electron spins are polarized by the pump light, whereas the noble-gas nuclear spins are polarized through the spin-exchange interactions with the alkali-metal spins. The precession of the polarized spin ensembles due to the external magnetic field and other excitations is typically measured by the probe light based on the interaction between the alkali-metal spins and the photons. The dynamics of the spin ensembles in the comagnetometer can be described by a set of Bloch equations [22–24], coupling the nuclear-spin polarization of noble-gas atoms $\mathbf{P^n}$ and the electron-spin polarization of alkali-metal atoms $\mathbf{P^e}$:

$$
\begin{aligned}
\frac{\partial \mathbf{P^e}}{\partial t} &= \frac{\gamma_e}{Q}\left(\mathbf{B} + \mathbf{B^n} + \mathbf{L} + \frac{\mathbf{\Omega}Q}{\gamma_e}\right) \times \mathbf{P^e} \\
&+ \frac{R_p\mathbf{S_p} + 2KR_{se}^{ne}\mathbf{P^n}}{Q} - \frac{\{R_1^e, R_2^e, R_2^e\}\mathbf{P^e}}{Q}, \\
\frac{\partial \mathbf{P^n}}{\partial t} &= \gamma_n\left(\mathbf{B} + \mathbf{B^e} + \frac{\mathbf{\Omega}}{\gamma_n}\right) \times \mathbf{P^n} + \frac{\varepsilon(K,\beta_n)}{2K}R_{se}^{en}\mathbf{P^e} \\
&- \{R_1^n, R_2^n, R_2^n\}\mathbf{P^n}.
\end{aligned}
\tag{1}
$$

In order, the first term in each equation describes the precession of each spin species in the sum of the external magnetic field $\mathbf{B}$, the effective magnetic field $\mathbf{B^e}$ ($\mathbf{B^n}$), and the inertial rotation $\mathbf{\Omega}$, whereas the alkali-metal spins additionally precess in the light shift $\mathbf{L}$. The light shift $\mathbf{L}$ can be eliminated by changing the pump-light frequency [25]; meanwhile, the inertial rotation $\mathbf{\Omega}$ is negligible on a stable platform. The electron and nuclear gyromagnetic ratios are given by γ_e and γ_n, respectively, whereas Q is the slowing-down factor [26]. The second term in each equation represents the polarizations of the alkali-metal and noble-gas spins, respectively. The alkali electron spins are polarized along the z axis by pumping light with rate R_p and photon polarization $\mathbf{S_p}$. Additionally, the alkali electron spins are also polarized by the spin-exchange interaction with the noble-gas atoms at rate R_{se}^{ne}, where K is the noble-gas nuclear spin. However, the rate R_{se}^{ne} can be ignored compared with R_p. Meanwhile the noble-gas nuclear spins are polarized along the z axis by the spin-exchange interaction with the alkali-metal atoms at rate R_{se}^{en}. Coefficient $\varepsilon(K,\beta_n)$ depends on K and the spin temperature β_n of the noble-gas spins [13]. The last term in each equation accounts for the relaxations of the longitudinal and transverse components of the polarization of alkali-metal spins (noble-gas spins) at rates R_1^e (R_1^n) and R_2^e (R_2^n), respectively.

The effective magnetic fields $\mathbf{B^e}$ and $\mathbf{B^n}$, experienced by one spin species owing to the magnetization of the other, are used to describe the dominant interaction between the spin-polarized noble-gas and alkali-metal atoms [22]. In a uniformly polarized spherical cell, the effective magnetic fields are represented by

$$
\begin{aligned}
\mathbf{B^n} &= \frac{2k\mu_0\mu_B n_n \mathbf{P^n}}{3}, \\
\mathbf{B^e} &= \frac{2k\mu_0\mu_B n_e \mathbf{P^e}}{3},
\end{aligned}
\tag{2}
$$

where k is the Fermi-contact-shift enhancement factor [14], μ_0 is the permeability of vacuum, μ_B is the Bohr magneton, and n_n and n_e are the densities of noble-gas and alkali-metal atoms, respectively.

When the excitation signal is relatively small, the longitudinal components of the polarizations, P_z^e and P_z^n, are nearly constant [19]. Usually, the transverse excitation signal should be one order of magnitude smaller than the sum of the holding magnetic field along the pumping direction and the relaxation rate of the alkali atoms. Thus, the Bloch equations can be linearized to obtain the transverse component of the polarization P_x^e [23]:

$$
P_x^e = P_1 e^{-\lambda_1 t} + P_2 e^{-\lambda_2 t} + P_x^{\text{steady}},
\tag{3}
$$

where parameters P_1, P_2, and P_x^{steady} depend on the inputting signals and initial conditions. The transient part of the P_x^e contains two oscillations, $\lambda_1 = \lambda_{1r} + i\lambda_{1i}$ and $\lambda_2 = \lambda_{2r} + i\lambda_{2i}$, corresponding to the precessions and decays of alkali-metal electrons and noble-gas nuclei transverse polarizations, respectively. The decay rates are

$$
\begin{aligned}
\lambda_{1r} &= \frac{R_2^e}{2Q} - \frac{\sqrt{\sqrt{a^2+b^2}+a}}{2\sqrt{2}}, \\
\lambda_{2r} &= \frac{R_2^e}{2Q} + \frac{\sqrt{\sqrt{a^2+b^2}+a}}{2\sqrt{2}}, \\
a &= \left(\frac{R_2^e}{Q}\right)^2 - \left[\frac{\gamma_e(B_z+B_z^n)}{Q} - \gamma_n B_z^e\right]^2 - \frac{4\gamma_e B_z^e \gamma_n B_z^n}{Q}, \\
b &= \frac{2R_2^e}{Q}\left(\frac{\gamma_e B_z + \gamma_e B_z^n}{Q} - \gamma_n B_z^e\right).
\end{aligned}
\tag{4}
$$

Here, the faster decay rate λ_{2r} corresponds to the decay rate of alkali-metal electron transverse polarization, whereas the slower decay rate λ_{1r} corresponds to the noble-gas nuclei [22,24]. In the absence of spin-exchange interactions, the noble-gas and alkali-metal spins would precess according to their own gyromagnetic ratios in the external magnetic field $\mathbf{B}$ and decay according to their own transverse relaxation rates. Usually, the precession frequency

and decay rate of noble-gas spins are significantly smaller than those of alkali-metal spins. However, when the two spin ensembles are coupled by the spin-exchange interactions in the low external magnetic field, the precession frequencies and decay rates become mixed. In particular, when the holding magnetic field along the z axis B_z is set to the fastest decay point B_z^f, the decay rate of noble-gas spins reaches the maximum [24]. This results from the fact that the motion of noble-gas nuclear spins is strongly coupled to the alkali-metal electron-spin motion; thus, the slower decay rate of the nuclear spins is accelerated by the faster decay rate of the electron spins [22,24]. Therefore, the entire spin ensembles exhibit a hybrid response and decays with the fastest rate. By setting $d\lambda_{1r}/dB_z = 0$, the fastest decay point is found to be

$$B_z^f = \frac{-B_z^n \gamma_e + B_z^e \gamma_n Q}{\gamma_e(1 - Q\gamma_n/\gamma_e)} \approx -B_z^n, \quad (5)$$

where the approximation is based on the reality that γ_e is 3–4 orders of magnitude larger than γ_n, Q is on the order of ten, and B_z^n is 1–2 orders of magnitude larger than B_z^e.

For quasisteady input signals, P_x^e can be approximated by the steady-state part,

$$P_x^e = \frac{\gamma_e P_z^e R_{\text{tot}}^e}{R_{\text{tot}}^{e\,2} + \gamma_e^2\,\delta B_z^2}\left[B_y\frac{\delta B_z}{B_z^n} + B_x\frac{\gamma_e\,\delta B_z^2}{R_{\text{tot}}^e B_z^n}\right], \quad (6)$$

where $\delta B_z = B_z + B_z^e + B_z^n$. When the holding magnetic field B_z is set to the compensation point, $B_z^c = -B_z^n - B_z^e$, δB_z equals zero; thus, the steady-state signal P_x^e is independent of the quasisteady input magnetic fields. This is because the nuclear magnetization of the noble gas would adiabatically compensate for any slowly changing magnetic field at the compensation point [8,22], leaving the alkali-metal electrons to experience a zero transverse magnetic field.

Therefore, by measuring the values of the fastest decay point B_z^f and the compensation point B_z^c, we can obtain B_z^n and B_z^e. According to Eq. (2), the polarizations P_z^n and P_z^e can then be calculated using the measured noble-gas and alkali-atom densities. The concrete procedure to measure B_z^n is as follows: scan the holding field B_z, measure the transient responses to a small step B_y, and fit the transient responses by Eq. (3) to obtain the slower decay rates λ_{1r}. Maximal λ_{1r} occurs at the fastest decay point; thus, the slower decay rates λ_{1r} of different B_z are fitted by Eq. (4) to obtain the corresponding $-B_z^n$ of the largest λ_{1r}. Meanwhile, the concrete procedure to measure B_z^e is as follows: scan the holding field B_z, measure the steady responses to a small step B_y, and fit the steady responses by Eq. (6). The compensation point $B_z^c = -B_z^n - B_z^e$ is found when the steady response equals zero; substitution of the measured B_z^n yields B_z^e. Above all, the transient and steady responses to a small step B_y are measured and fitted to obtain B_z^n and

B_z^e, which are then used to calculated the polarizations P_z^n and P_z^e based on Eq. (2), respectively.

III. EXPERIMENTAL SETUP AND RESULTS

This method is performed on a K-Rb-^{21}Ne comagnetometer shown in Fig. 1. A spherical cell made of aluminosilicate glass (GE180) is filled with a small mixed droplet of K-Rb metal, 2280-torr ^{21}Ne (70%-isotope enriched), and 52-torr N_2 gases at 25°C (referred to as cell 1) and installed in a boron-nitride oven, which is heated by a 110-kHz ac electric heater. The molar fraction of K f_K in cell 1 is kept small to improve the polarization homogeneity [27]. The density of Rb, n_{Rb}, is calculated based on the saturated density and Raoult's law [27], with the temperature monitored by the platinum resistor pasted on the cell, and further verified based on the laser-absorption-spectroscopy method. Meanwhile, the density of ^{21}Ne, n_{Ne}, is measured during the gas-filling process by the vacuum gauge. Three-axis magnetic field coils generate uniform fields in each direction. The magnetic field shields consist of five layers of μ-metal barrels, providing a shielding factor better than 1×10^6 and a remanent magnetic field smaller than 2 nT in three directions after degaussing. A 1.5-W pump light of the K D_1 line, (Toptica TA pro) is circularly polarized and expanded to polarized K atoms. The P_x^e of the Rb electron spins is measured by a linearly polarized and red-detuned (0.4-nm) probe light of the Rb D_1 line from a distributed-feedback laser based on optical rotation and converted to a voltage signal $S_x^e = AP_x^e$ by a scale factor A. To reduce low-frequency noise, the probe light is modulated by a photoelastic modulator (Hinds Instruments PEM100) and then demodulated by a lock-in amplifier (Zurich Instruments HF2LI).

First, to present the change in the dynamics of the spin ensembles with holding magnetic field B_z, the relationships
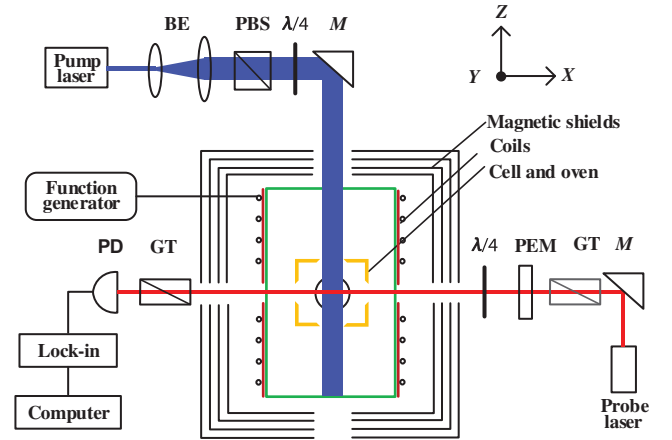

FIG. 1.   The experimental setup of the comagnetometer: BE, beam expander; PBS, polarization beam splitter; M, mirror; GT, Glan-Taylor polarizer; PD, photodetector.
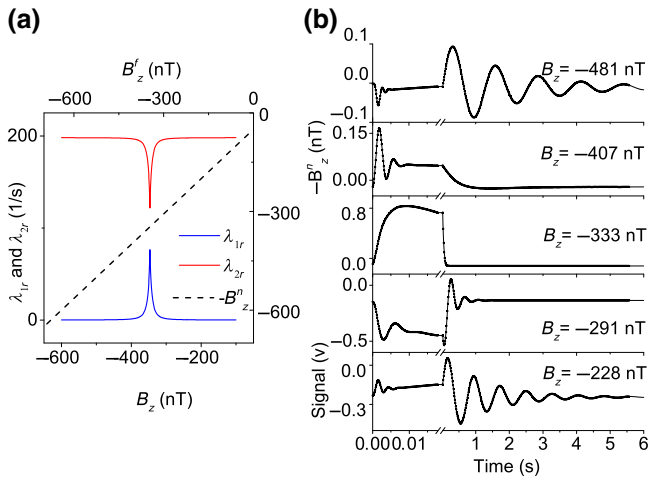
(a)

(b)

FIG. 2.　(a) The solid curves are the simulated decay rates and are plotted against the bottom-*x*, left-*y* coordinate, whereas the dashed line is the simulated relationship between B_z^f and $-B_z^n$, plotted against the top-*x*, right-*y* coordinate. (b) The dots are measured transient signals with different B_z and fitted by the curves based on Eq. (3). To present the faster decay precession clearly, the *x* axis is broken into two parts, in which the first part extends from 0 to 18 ms and the second part goes from 18 ms to 6 s.

between the two decay rates and the holding magnetic field B_z are simulated based on Eq. (4) in Fig. 2(a). The simulation is based on the K-Rb-^{21}Ne cell mentioned above, with a typical temperature 180°C and typical Rb polarization $P_z^e = 0.6$. Using the parameters in Ref. [13], the effective magnetic fields are calculated to be $B_z^n = 296.8$ nT and $B_z^e = 46.7$ nT. When the holding field B_z is far away from the fastest decay point, $B_z^f = -B_z^n = -296.8$ nT, the decay rate of the Rb electron spins λ_{2r} is significantly larger than that of the ^{21}Ne nuclear spins λ_{1r}. Close to the fastest decay point, λ_{2r} decreases while λ_{1r} increases, causing the decay rates to become coupled. At the fastest decay point, λ_{2r} and λ_{1r} reach their smallest and largest values, respectively. Because the damping time of the precession signal is determined by the slower decay rate λ_{1r}, the procession signal decays with the fastest rate at the fastest decay point. In addition, to verify the validity of the approximation in Eq. (5), the values of the fastest decay point B_z^f of different temperatures and pump-light intensities are numerically calculated based on Eq. (4) and compared with the approximate results of Eq. (5), $-B_z^n$. As shown in the top-*x*, right-*y* coordinate in Fig. 2(a) by the dashed line, the numerically calculated B_z^f are consistent with the approximate results $-B_z^n$, which means that the approximation in Eq. (5) is reasonable.

Next, we present the measurement of the fastest decay point and the compensation point by measuring the transient and steady responses to determine the spin polarizations. Figure 2(b) shows the measured transient responses to a small-step magnetic field B_y for several values of

the holding field B_z with temperature 190°C and pump-light intensity 339.6 mW/cm². When the B_z is away from the fastest decay point $B_z^f = -B_z^n = -353.2$ nT, there are two separated decaying oscillations λ_1 and λ_2 in the transients, as indicated in Eq. (3). As B_z approaches the fastest decay point, the two decaying oscillations gradually become matched. At the fastest decay point, the two spin species are strongly coupled and the precession signal decays at the fastest rate. The transient responses are fitted using Eq. (3) and the fitting curves are in good agreement with the measured data.

The slower decay rates λ_{1r}, obtained by fitting the transients with Eq. (3), are summarized in Fig. 3(a) and fitted by the solid curve based on Eq. (4). The maximum value of the fitting curve appears at the fastest decay point, $B_z^f = -B_z^n = -353.2$ nT. After determining B_z^n, we measure the compensation point to obtain B_z^e. Scanning the holding field B_z, the difference ΔS_x^e between steady signals before and after a step magnetic field applied along the *y* axis, $B_y = 0.48$ nT, is measured and shown in Fig. 3(b). The measured data are consistent with the solid fitting curve based on Eq. (6), with the coefficient of determination R^2 (the goodness of fit) of 0.9997. At the compensation point $B_z^c = -430.1$ nT, ΔS_x^e equals zero, as predicted by Eq. (6). Based on the measured B_z^f and B_z^c, the effective magnetic fields of ^{21}Ne and Rb atoms are $B_z^n = -B_z^f = 353.2$ nT and $B_z^e = -B_z^c + B_z^f = 82.7$ nT, respectively. Based on Eq. (2) and $k = 35.7 \pm 3.7$ [14], the corresponding polarizations of the ^{21}Ne nuclear and Rb electron spins are $P_z^n = 0.057 \pm 0.006$ and $P_z^e = 0.48 \pm 0.05$, respectively.

To verify the validity of this method under different conditions, the polarizations of the Rb and ^{21}Ne spins are measured with different pump-light intensities and temperatures and compared with the theoretical model. With several different pump-light intensities and temperatures, the values of the fastest decay point and the compensation point are measured and shown in Fig. 4(a), whereas the corresponding polarizations are plotted in Fig. 4(b). The equilibrium spin polarization of Rb is $P_z^e =$
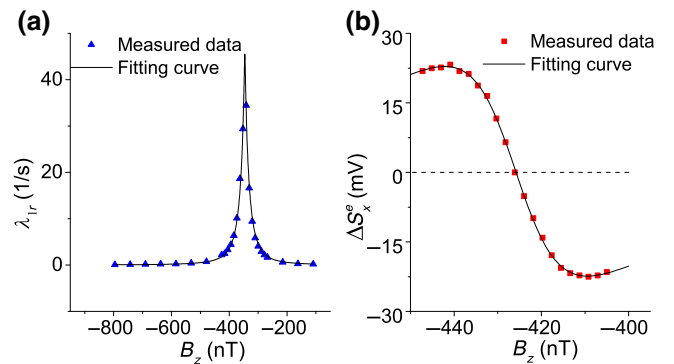
(a)

(b)

FIG. 3.　The measured λ_{1r} and ΔS_x^e as functions of the holding magnetic field. The dots are the measured data and are fitted by the solid curves.
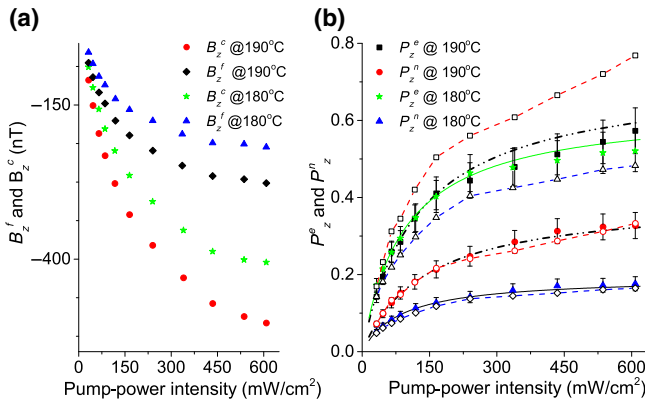
FIG. 4. The measured B_z^f and B_z^c and the corresponding polarizations of Rb and ^{21}Ne atoms at various pump-light intensities and temperatures. (a) The measured B_z^f and B_z^c under different conditions. (b) The dotted data are the measured P_z^e and P_z^n. The solid curves are fitting lines based on $y = Kx/(x + a)$ for P_z^e and P_z^n at 180°C, while the dash-dotted fitting curves are for P_z^e and P_z^n at 190°C. The dashed curves with hollow squares and triangles are the theoretically calculated results for P_z^n at 190°C and 180°C, respectively, which are based on the measured $P_z^n = 5 R_{se}^{en} / (3 R_{se}^{en} + 3 R_{rel}^{n}) P_z^e$ without consideration of the magnetic field gradient relaxation, while the dashed curves with hollow circles and diamonds are the theoretically calculated results for P_z^n at 190°C and 180°C, respectively, with consideration of the magnetic field gradient relaxation. All P_z^n are scaled up 5 times for clarity.

$R_p / (R_p + R_{rel}^e)$, where R_{rel}^e is the longitudinal relaxation rate of Rb, excluding the R_p. The equilibrium nuclear-spin polarization of ^{21}Ne is small under our experimental conditions; hence, the coefficient $\varepsilon(3/2, \beta_n)$ is approximately equal to 5 [13] and the equilibrium polarization is $P_z^n = 5 R_{se}^{en} / (3 R_{se}^{en} + 3 R_{rel}^{n}) P_z^e$, where R_{rel}^n is the longitudinal relaxation rate of ^{21}Ne, excluding the R_{se}^{en}. Therefore, the measured polarizations P_z^e and P_z^n can be fitted by $y = Kx/(x + a)$ with different values of K, where x is the pump-light intensity, proportional to R_p, and a is proportional to R_{rel}^e. In Fig. 4(b), the measured P_z^e and P_z^n are fitted well based on $y = Kx/(x + a)$ by the solid curves and dash-dotted curves, respectively. $a = 93.5$ for fitting P_z^e is consistent with $a = 86.3$ for P_z^n at 180°C and $a = 123.0$ for fitting P_z^e also agrees with $a = 139.1$ for P_z^n at 190°C. However, when the pump power is high, there are differences between the measured P_z^e and the fitting curves. This results from the fact that the strong pump light heats the cell and causes the R_{rel}^e to increase; therefore, the fitting data are larger than the measured P_z^e at the high pump power.

As a further check, based on the theoretically calculated R_{se}^{en} and R_{rel}^n [13,14], the P_z^n, calculated by the measured P_z^e using $P_z^n = 5 R_{se}^{en} / (3 R_{se}^{en} + 3 R_{rel}^{n}) P_z^e$, are compared to the measured P_z^n. As shown in Fig. 4(b), the calculated P_z^n are shown by the dashed curve with hollow squares

for 190°C and by another dashed curve with hollow triangles for 180°C. These calculated P_z^n are larger than the measured data, because we consider that the R_{rel}^n is mainly contributed by the quadruple relaxation [13], with the other relaxations, such as the magnetic field gradient relaxation, neglected. If the gradient relaxations due to the residual magnetic field gradient, the polarization gradient, and the nonspherical cell are taken into account with, for example, a transverse magnetic field gradient of approximately 3–4 nT/cm and a holding magnetic field of approximately 100–200 nT [28], the calculated P_z^n (dashed curves with hollow circles and diamonds) are identical to the measured data.

In addition, another K-Rb-^{21}Ne cell with a higher molar fraction of K (referred to as cell 2) is used to measure the Rb spin polarization based on our method at 180°C and to compare with the traditional FSNP method. The brief principle of the FSNP method is that the transverse polarization of noble-gas nuclear spins introduced by a tipping pulse would precess in the sum of the holding field B_z and the effective magnetic field B_z^e. When the polarization of alkali-metal spins is reversed by changing the polarity of the circularly polarized pump light, the precession frequency of the noble-gas spins is shifted by $\Delta f_n = 2 \gamma_n B_z^e$. Therefore, the effective field B_z^e can be acquired by measuring the frequency shift [21]. In Fig. 5, the effective magnetic fields B_z^e measured by these two methods are plotted against the left y axis, whereas the corresponding polarizations are plotted against the right y axis. The results of these two methods are consistent with each other at different pump-light intensities. The maximal difference between the polarizations measured by these two methods at the same pump-light intensity is 0.04. Likewise, the fitting data are larger than the measured P_z^e at the high pump power due to the heating effect of the strong pump light.

The measurement uncertainty of this method consists of systematic uncertainty (type B) and random uncertainty
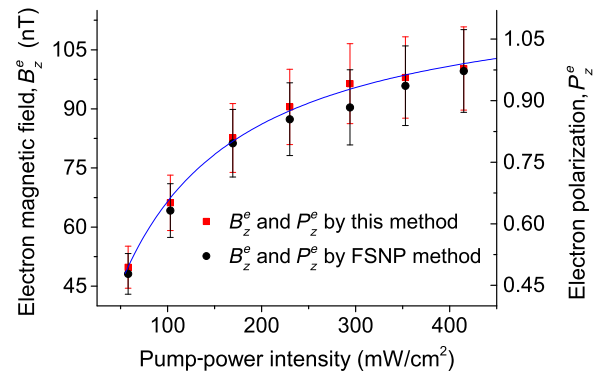

FIG. 5. A comparison between the polarizations measured by our method and that of the FSNP method. The blue solid curve is the fitting curve of the measured polarizations based on our method.

(type A). The systematic uncertainty arises from the uncertainty of the Fermi-contact-shift enhancement factor k and the uncertainty of the approximation of B_z^f in Eq. (5), as well as the uncertainties due to the cell geometry and the nonuniform spin polarization. The relative uncertainty of k is measured to be 10.4% [14], whereas the uncertainty of the approximation of B_z^f is smaller than 1%.

In general, the effective magnetic field $\mathbf{B^e}$ ($\mathbf{B^n}$) in Eq. (2) is composed of the Fermi-contact interaction term and the classical magnetization term [13,22,29]. The Fermi-contact enhancement factor k in Eq. (2) should be modified to be $k = k_0' + k_c$, where k_0' and k_c correspond to the Fermi-contact interaction term and the classical magnetization term, respectively [15,29]. By modifying the factor k_c for different cell geometries, the $\mathbf{B^e}$ and $\mathbf{B^n}$ in Eq. (2) can be extended to the nonspherical cell, even for a cell with an appendage or stem [13,29]. On the one hand, the k_0' for Rb-^{21}Ne is 34.7 ± 3.7 [13], while k_c is on the order of unity for a nonspherical cell ($k_c = 1$ for a uniformly polarized spherical cell). The contribution of the classical magnetization term to the effective magnetic field is one order of magnitude smaller than the Fermi-contact interaction term. On the other hand, the main nonspherical part of our cells is the cylindrical pull-off stem, which is very small, with a length of 0.5 cm and an inner diameter of 0.15 cm. The stem volume is only about 1% of the total cell volume. Therefore, the uncertainty arising from the cell geometry is less than 1% due to the large k_0' and the small nonspherical volume [30].

An inhomogeneous laser intensity and attenuation of the laser through the cell can both give rise to nonuniform alkali electron-spin polarization P_z^e. However, due to the fast spin-exchange rate between electron spins and the same electron-spin polarization in both hyperfine states, the alkali electron spins do not see any torque due to their own spin polarization [22]. As for the effect of the nonuniform P_z^e on the noble-gas nuclear spins, because the diffusion time of ^{21}Ne nuclear spins ($\tau_d \approx d^2/6D_{Ne} \approx 558$ ms at 180°C in our case) is about 3–4 orders of magnitude shorter than the spin-exchange time of the Rb-^{21}Ne pair and the relaxation time of the ^{21}Ne, the nuclear spins experience a volume-averaged P_z^e, i.e., the B_z^e experienced by the nuclear spins is volume averaged [22,30]. Therefore, this method measures the volume-averaged P_z^e. Likewise, a nonuniform alkali-metal density and electron-spin polarization could potentially cause the inhomogeneity of P_z^n. However, P_z^n is uniform because the diffusion time is much shorter than the relaxation rate [30] and thus the effect of the inhomogeneity of P_z^n is negligible. The uncertainty due to a nonuniform P_z^e arises from the approximation of the volume-averaged classical magnetization term in B_z^e with Eq. (2) [15,31]. In our case, the contribution of the classical magnetization term to the total B_z^e is 1/35.7, which means that this error is less than 3% even for the extreme case.

In addition, to estimate the P_z^e inhomogeneity, we have added the three-dimensional (3D) numerical simulation of the P_z^e, taking the cell geometry, the wall relaxation, and the nonuniform pump laser into consideration. This simulation is based on the finite-element method, which is applied for the polarization simulation of Rb-^{129}Xe in Ref. [32,33]. The parameters of the K-Rb-^{21}Ne cell used in the simulation can be found in Ref. [13,34] and the pump light emitted from the single-mode polarization-maintaining fiber is calculated as the Gaussian distribution with a beam diameter of 18 mm. Simulations of the P_z^e in cell 1 with a temperature of 180°C and a pump-light power of 30 mW are shown in Figs. 6(a) and 6(b). The inhomogeneity due to the nonuniform pump laser and the cell geometry can be seen in the cross section of the x-y plane at $z = 0$ in Fig. 6(a), while the inhomogeneity due to the light absorption across the cell is shown in the cross section of the y-z plane at $x = 0$ in Fig. 6(b). To describe the polarization inhomogeneity, we define a dimensionless factor, the homogeneity ratio, which is the ratio of the volume-averaged polarization to the maximum polarization in the cell. The homogeneity ratio under different experimental conditions of cell 1 is plotted in Fig. 6(c). The P_z^e is more uniform for the situation with a lower temperature and a higher pump-light power due to the weaker light absorption and higher electron-spin polarization, this being identical to the analytical result in Ref. [34]. The simulated P_z^e are higher than the corresponding measured values, which results from the fact that the actual incident pump-power values going into the cell are smaller than those measured outside of the vacuum window, and the actual relaxation rates of the alkali atoms are higher than the theoretically calculated values.
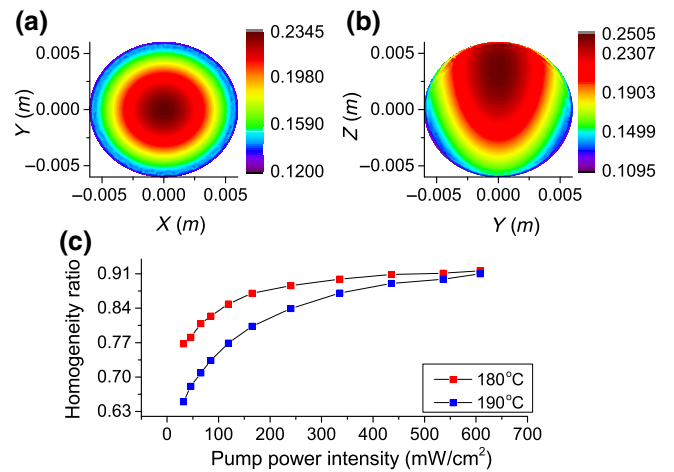

FIG. 6. The 3D simulation of P_z^e. (a) The cross section of the x-y plane at $z = 0$ with a temperature of 180°C and a pump-light power of 30 mW. (b) The cross section of the y-z plane at $x = 0$ with a temperature of 180°C and a pump-light power of 30 mW. (c) The calculated homogeneity ratios with different temperatures and pump power densities.

The random uncertainty arises from the measurements of the compensation point B_z^c, the fastest decay point B_z^f, and the densities of Rb and ^{21}Ne atoms. The B_z^f and B_z^c are acquired by fitting the transient and steady responses to the step magnetic field with relative uncertainties smaller than 2%. During the gas-filling process, the density of ^{21}Ne, n_{Ne}, is obtained by measuring the pressure in the tube using a vacuum gauge before the glass cell is pulled off the tube and then further checked by measuring the remaining gas pressure after the cell is pulled off the tube. We estimate the relative uncertainty of n_{Ne} to be less than 5%.

A spherical cell filled with pure K metal and 3 atm of ^{4}He (referred to as cell 3) is used to calibrate the molar fraction of K atoms in cells 1 and 2 based on the laser-absorption-spectroscopy method (LAS). According to Raoult's law, the molar fraction of K atoms in the hybrid cell is $f_K = n_K/n_{K1}$, where n_K is the K density in the hybrid cell measured by LAS, n_{K1} being the K density of the pure K cell measured by LAS at the same condition instead of the calculated saturated density, to avoid the measurement error of the cell temperature. As shown in Fig. 7(a), the laser-absorption curves of cells 1 and 3 measured at different temperatures are fitted to obtain the densities [34]. In Fig. 7(b), the calculated K molar fraction of cell 1 at different temperatures is averaged to be $f_K = 0.072 \pm 0.004$, while the average of the K molar fraction in cell 2 is

$f_K = 0.289 \pm 0.009$. Because the molar fraction of K f_K remains constant in the sealed cell under our operating conditions, the densities $n_K = f_K n_{K0}$ and $n_{Rb} = (1 - f_K)n_{Rb0}$ can be obtained by substituting in the saturated densities n_{K0} and n_{Rb0}, which are calculated based on the directly measured cell temperature. However, the calculated densities will be different from the true values due to the operating conditions, especially the strong pump light and temperature gradient. Thus, it is necessary to measure the densities under the operating conditions. The density of K atoms, which is optical thin in the hybrid cell at high temperature, is measured under the operating conditions based on LAS to obtain the effective temperature, and then used to to deduce the Rb density. In Figs. 7(c) and 7(d), the measured effective temperatures of cells 1 and 2 increase significantly with the pump-light power. The uncertainty of n_{Rb} mainly derives from the uncertainties of the molar fraction and the effective cell temperature. Under the operating conditions, the uncertainty of n_{Rb}, which is calculated based on the measured molar fraction and the effective temperature, is smaller than 5.5% for cell 1 and 4.7% for cell 2. There are also many other methods to directly measure the density of the optically thick Rb atoms to improve the accuracy [13,35]. To sum up, the total extended measurement uncertainties of P_z^e and P_z^n are less than 12.4%. The uncertainties of k and the densities are the two largest uncertainties of this method and they are also the challenging terms for the traditional methods [15,16,21].

IV. CONCLUSION

We demonstrate a method for simultaneously measuring the spin polarizations of noble-gas and alkali-metal atoms based on the dynamics of the spin ensembles. Under the normal operation conditions of the K-Rb-^{21}Ne comagnetometer, the polarizations of the Rb and ^{21}Ne spins are measured by this method and found to be consistent with the theoretical model. This method can also be applied in a wider operating range. Additionally, the traditional FSNP method is used to further verify the validity of this method. Although the accuracy of this method is limited by the uncertainty of k, it has the advantage of simultaneous measurement of polarizations, simplifying the previous separated measurement procedures. Furthermore, owing to the simplified configuration, it is suitable for miniaturized devices. The method can be extended to measure other alkali-metal and noble-gas species enclosed in other geometrically configured cells. In addition, because this method will not depolarize the noble-gas or alkali-metal spins, it can be used in real-time polarization measurement.
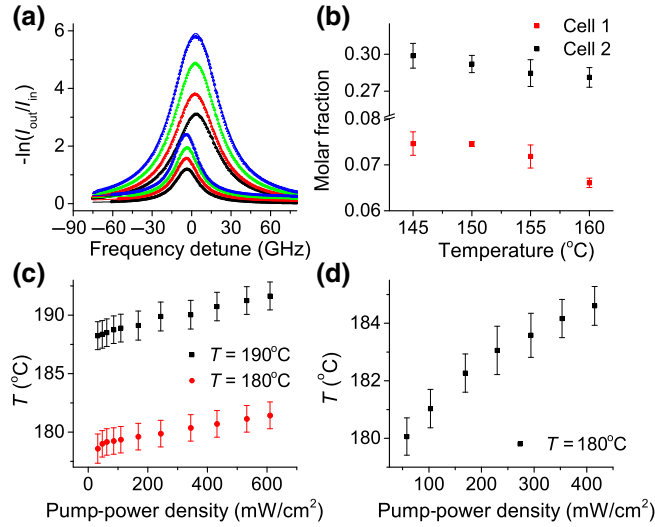

FIG. 7. (a) The top four curves are the laser-absorption curves of cell 3 at 160°C, 155°C, 150°C, and 145°C, respectively, while the bottom four curves are those for of cell 1 at 160°C, 155°C, 150°C, and 145°C, respectively. The vertical axis is $-Ln(I_{out}/I_{in})$, where I_{in} and I_{out} are the incident and transmitted light intensities, respectively. The zero point of the horizontal axis is the D_1 line of K in vacuum. The curves of cell 1 are scaled up 5 times for clarity. (b) The measured molar fraction of K in cells 1 and 2 at different temperatures. (c),(d) The calculated effective temperatures T under the operating conditions of cells 1 and 2, respectively.

[1] D. Budker and M. V. Romalis, Optical magnetometry, Nat. Phys. **3**, 227 (2007).

[2] M. Smiciklas, J. M. Brown, L. W. Cheuk, S. J. Smullin, and M. V. Romalis, New Test of Local Lorentz Invariance Using a K-Rb-^{21}Ne Comagnetometer, Phys. Rev. Lett. **107**, 171604 (2011).

[3] W. Ji, Y. Chen, C. B. Fu, M. Ding, J. C. Fang, Z. G. Xiao, K. Wei, and H. Y. Yan, New Experimental Limits on Exotic Spin-Spin-Velocity-Dependent Interactions by Using SmCo$_5$ Spin Sources, Phys. Rev. Lett. **121**, 261803 (2018).

[4] J. Y. Lee, A. Almasi, and M. Romalis, Improved Limits on Spin-Mass Interactions, Phys. Rev. Lett. **120**, 161801 (2018).

[5] M. Rao, N. J. Stewart, G. Norquay, P. D. Griffiths, and J. M. Wild, High resolution spectroscopy and chemical shift imaging of hyperpolarized ^{129}Xe dissolved in the human brain *in vivo* at 1.5 tesla, Magn. Reson. Med. **75**, 2227 (2016).

[6] J. P. Mugler, III and T. A. Altes, Hyperpolarized ^{129}Xe MRI of the human lung, J. Magn. Reson. Imaging **37**, 313 (2013).

[7] C. Y. Jiang, X. Tong, D. R. Brown, S. Chi, A. D. Christianson, B. J. Kadron, J. L. Robertson, and B. L. Winn, Development of a compact *in situ* polarized ^{3}He neutron spin filter at Oak Ridge National Laboratory, Rev. Sci. Instrum. **85**, 075112 (2014).

[8] T. W. Kornack, R. K. Ghosh, and M. V. Romalis, Nuclear Spin Gyroscope Based on an Atomic Comagnetometer, Phys. Rev. Lett. **95**, 230801 (2005).

[9] R. J. Li, W. F. Fan, L. W. Jiang, L. H. Duan, W. Quan, and J. C. Fang, Rotation sensing using a K-Rb-^{21}Ne comagnetometer, Phys. Rev. A **94**, 032109 (2016).

[10] J. C. Fang, Y. Chen, S. Zou, X. J. Liu, Z. H. Hu, W. Quan, H. Yuan, and M. Ding, Low frequency magnetic field suppression in an atomic spin co-magnetometer with a large electron magnetic field, J. Phys. B: At. Mol. Opt. Phys. **49**, 065006 (2016).

[11] E. Babcock, B. Chann, T. G. Walker, W. C. Chen, and T. R. Gentile, Limits to the Polarization for Spin-Exchange Optical Pumping of ^{3}He, Phys. Rev. Lett. **96**, 083003 (2006).

[12] B. Lancor and T. G. Walker, Polarization limits in K-Rb spin-exchange mixtures, Phys. Rev. A **83**, 065401 (2011).

[13] R. K. Ghosh, Ph.D. thesis, Department of Physics, Princeton University, Princeton, NJ, USA, 2009.

[14] R. K. Ghosh and M. V. Romalis, Measurement of spin-exchange and relaxation parameters for polarizing ^{21}Ne with K and Rb, Phys. Rev. A **81**, 043415 (2010).

[15] M. V. Romalis and G. D. Cates, Accurate ^{3}He polarimetry using the Rb Zeeman frequency shift due to the Rb $-^3$He spin-exchange collisions, Phys. Rev. A **58**, 3004 (1998).

[16] B. Chann, E. Babcock, L. W. Anderson, and T. G. Walker, Measurements of ^{3}He spin-exchange rates, Phys. Rev. A **66**, 032703 (2002).

[17] A. B. Baranga, S. Appelt, C. J. Erickson, A. R. Young, and W. Happer, Alkali-metal-atom polarization imaging in high-pressure optical-pumping cells, Phys. Rev. A **58**, 2282 (1998).

[18] A. R. Young, S. Appelt, A. B. Baranga, C. Erickson, and W. Happer, Three-dimensional imaging of spin polarization of alkali-metal vapor in optical pumping cells, Appl. Phys. Lett. **70**, 3081 (1997).

[19] M. V. Romalis, Hybrid Optical Pumping of Optically Dense Alkali-Metal Vapor Without Quenching Gas, Phys. Rev. Lett. **105**, 243001 (2010).

[20] B. Lancor, E. Babcock, R. Wyllie, and T. G. Walker, Circular dichroism of RbHe and RbN$_2$ molecules, Phys. Rev. A **82**, 043435 (2010).

[21] J. Y. Lee, Ph.D. thesis, Department of Physics, Princeton University, Princeton, NJ, USA, 2019.

[22] T. W. Kornack and M. V. Romalis, Dynamics of Two Overlapping Spin Ensembles Interacting by Spin Exchange, Phys. Rev. Lett. **89**, 253002 (2002).

[23] W. Quan, K. Wei, and H. R. Li, Precision measurement of magnetic field based on the transient process in a K-Rb-^{21}Ne comagnetometer, Opt. Express **25**, 8470 (2017).

[24] J. C. Fang, Y. Chen, Y. Lu, W. Quan, and S. Zou, Dynamics of Rb and ^{21}Ne spin ensembles interacting by spin exchange with a high Rb magnetic field, J. Phys. B: At. Mol. Opt. Phys. **49**, 135002 (2016).

[25] Y. Chen, W. Quan, L. H. Duan, Y. Lu, L. W. Jiang, and J. C. Fang, Spin-exchange collision mixing of the K and Rb ac Stark shifts, Phys. Rev. A **94**, 052705 (2016).

[26] I. M. Savukov and M. V. Romalis, Effects of spin-exchange collisions in a high-density alkali-metal vapor in low magnetic fields, Phys. Rev. A **71**, 023405 (2005).

[27] E. Babcock, I. Nelson, S. Kadlecek, B. Driehuys, L. W. Anderson, F. W. Hersman, and T. G. Walker, Hybrid Spin-Exchange Optical Pumping of ^{3}He, Phys. Rev. Lett. **91**, 123003 (2003).

[28] G. D. Cates, S. R. Schaefer, and W. Happer, Relaxation of spins due to field inhomogeneities in gaseous samples at low magnetic fields and low pressures, Phys. Rev. A **37**, 2877 (1988).

[29] E. D. Babcock, Ph.D. thesis, University of Wisconsin-Madison, Madison, WI, USA, 2005.

[30] Z. L. Ma, E. G. Sorte, and B. Saam, Collisional ^{3}He and ^{129}Xe Frequency Shifts in Rb–Noble-Gas Mixtures, Phys. Rev. Lett. **106**, 193005 (2011).

[31] S. R. Schaefer, G. D. Cates, T.-R. Chien, D. Gonatas, W. Happer, and T. G. Walker, Frequency shifts of the magnetic-resonance spectrum of mixtures of nuclear spin-polarized noble gases and vapors of spin-polarized alkali-metal atoms, Phys. Rev. A **39**, 5613 (1989).

[32] A. Fink, D. Baumer, and E. Brunner, Production of hyperpolarized xenon in a static pump cell: Numerical simulations and experiments, Phys. Rev. A **72**, 053411 (2005).

[33] Y. C. Jia, Z. C. Liu, B. Q. Zhou, X. Y. Liang, W. F. Wu, J. P. Peng, M. Ding, Y. Y. Zhai, and J. C. Fang, Pump beam

influence on spin polarization homogeneity in the nuclear magnetic resonance gyroscope, J. Phys. D: Appl. Phys. **52,** 355001 (2019).

[34] S. J. Seltzer, Ph.D. thesis, Department of Physics, Princeton University, Princeton, NJ, USA, 2008.

[35] H. Zhang, S. Zou, X. Y. Chen, M. Ding, G. C. Shan, Z. H. Hu, and W. Quan, On-site monitoring of atomic density number for an all-optical atomic magnetometer based on atomic spin exchange relaxation, Opt. Express **24,** 17234 (2016).